



**HAL**  
open science

## **A Versatile G-quadruplex (G4)-coated Upconverted Metal-Organic Framework for Hypoxic Tumor Therapy**

Xuanxiang Mao, Xiaobo Zhang, Zhicong Chao, Dehui Qiu, Shijiong Wei, Rengan Luo, Desheng Chen, Yue Zhang, Yun Chen, Yuanjiao Yang, et al.

### ► To cite this version:

Xuanxiang Mao, Xiaobo Zhang, Zhicong Chao, Dehui Qiu, Shijiong Wei, et al. A Versatile G-quadruplex (G4)-coated Upconverted Metal-Organic Framework for Hypoxic Tumor Therapy. *Advanced Healthcare Materials*, In press, 10.1002/adhm.202300561 . hal-04152890v1

**HAL Id: hal-04152890**

**<https://hal.science/hal-04152890v1>**

Submitted on 5 Jul 2023 (v1), last revised 10 Aug 2023 (v2)

**HAL** is a multi-disciplinary open access archive for the deposit and dissemination of scientific research documents, whether they are published or not. The documents may come from teaching and research institutions in France or abroad, or from public or private research centers.

L'archive ouverte pluridisciplinaire **HAL**, est destinée au dépôt et à la diffusion de documents scientifiques de niveau recherche, publiés ou non, émanant des établissements d'enseignement et de recherche français ou étrangers, des laboratoires publics ou privés.

# A Versatile G-quadruplex (G4)-coated Upconverted Metal-Organic Framework for Hypoxic Tumor Therapy

Xuanxiang Mao,<sup>1</sup> Xiaobo Zhang,<sup>1</sup> Zhicong Chao,<sup>1</sup> Dehui Qiu,<sup>1</sup> Shijiong Wei,<sup>1</sup> Rengan Luo,<sup>1</sup> Desheng Chen,<sup>1</sup> Yue Zhang,<sup>2</sup> Yun Chen,<sup>1</sup> Yuanjiao Yang,<sup>1</sup> David Monchaud,<sup>3</sup> Huangxian Ju,<sup>1</sup> Jean-Louis Mergny,<sup>1,4,\*</sup> Jianping Lei,<sup>1</sup> Jun Zhou<sup>1,\*</sup>

<sup>1</sup> State Key Laboratory of Analytical Chemistry for Life Science, School of Chemistry and Chemical Engineering, Nanjing University, Nanjing 210023, PR China.

<sup>2</sup> School of Pharmacy, Nanjing University of Chinese Medicine, Nanjing 210023, PR China.

<sup>3</sup> Institut de Chimie Moléculaire (ICMUB), CNRS UMR6302, UBFC, 21078 Dijon, France.

<sup>4</sup> Laboratoire d'Optique et Biosciences (LOB), Ecole Polytechnique, CNRS, INSERM, Institut Polytechnique de Paris, 91128 Palaiseau, France.

X. M. and X. Z. are joint first authors.

\*Corresponding authors:

Jean-Louis Mergny [jean-louis.mergny@polytechnique.edu](mailto:jean-louis.mergny@polytechnique.edu)

Jun Zhou [jun.zhou@nju.edu.cn](mailto:jun.zhou@nju.edu.cn)

Coauthors emails:

Xuanxiang Mao: [DG1924064@smail.nju.edu.cn](mailto:DG1924064@smail.nju.edu.cn); Xiaobo Zhang: [xhzb@nju.edu.cn](mailto:xhzb@nju.edu.cn);

Zhicong Chao: [DG21240005@smail.nju.edu.cn](mailto:DG21240005@smail.nju.edu.cn); Dehui Qiu: [xhqdh@smail.nju.edu.cn](mailto:xhqdh@smail.nju.edu.cn);

Shijiong Wei: [weishijiong@smail.nju.edu.cn](mailto:weishijiong@smail.nju.edu.cn); Rengan Luo:

[DZ1824023@smail.nju.edu.cn](mailto:DZ1824023@smail.nju.edu.cn); Desheng Chen: [971059738@qq.com](mailto:971059738@qq.com); Yue Zhang:

[zhangyue035@njucm.edu.cn](mailto:zhangyue035@njucm.edu.cn); Yun Chen: [njuchenyun@qq.com](mailto:njuchenyun@qq.com); Yuanjiao Yang:

[yangyuanjiao@smail.nju.edu.cn](mailto:yangyuanjiao@smail.nju.edu.cn); David Monchaud: [david.monchaud@u-bourgogne.fr](mailto:david.monchaud@u-bourgogne.fr);

Huangxian Ju: [hxju@nju.edu.cn](mailto:hxju@nju.edu.cn); Jianping Lei: [jpl@nju.edu.cn](mailto:jpl@nju.edu.cn)

## Abstract

Given the complexity of the tumor microenvironment, multiple strategies are being explored to tackle hypoxic tumors. One of the most efficient strategies combines several therapeutic modalities and typically requires the development of multifunctional nanocomposites through sophisticated synthetic procedures. Here, the G-quadruplex (G4)-forming sequence AS1411-A (d-(G<sub>2</sub>T)<sub>4</sub>TG(TG<sub>2</sub>)<sub>4</sub>A) was designed and used for its anti-tumor and biocatalytic properties, such as increasing the production of O<sub>2</sub> *ca.* 2-fold as compared to the parent AS1411 sequence. Subsequently, the AS1411-A/hemin complex (GH) was grafted on the surface and pores of a core-shell upconverted metal-organic framework (UMOF) to generate a UMGH nanoplatfom. Compared with UMOF, UMGH exhibited enhanced colloidal stability, increased targeting of tumor cells and improved O<sub>2</sub> production (8.5-fold) *in situ*. When irradiated with near-infrared (NIR) light, the UMGH antitumor properties were bolstered by photodynamic therapy (PDT), thanks to its ability to convert O<sub>2</sub> into singlet oxygen (<sup>1</sup>O<sub>2</sub>). Combined with the antiproliferative activity of AS1411-A, this novel approach herein lays the foundation for a new type of G4-based nanomedicine.

**Keywords:** G-quadruplex; G-quadruplex/hemin; upconverted metal-organic framework; photodynamic therapy; antiproliferative activity.

## 1. Introduction

G-Quadruplexes (G4s) are four-stranded structures formed by guanine-rich strands which have emerged as a subject of intense interest in fields as diverse as cell biology, chemical biology and bionanotechnology.<sup>[1]</sup> G4-forming sequences are abundantly present in both the human genome and transcriptome, thereby making them a popular subject for genetic research in order to investigate their associated cellular functions.<sup>[2]</sup> G4s have also been used to create nanodevices, which have been effectively implemented as artificial enzymes, biosensors and drug carriers.<sup>[3]</sup> For instance, several G4 aptamers, such as AS1411,<sup>[4]</sup> TBA,<sup>[5]</sup> apMNK,<sup>[6]</sup> S13,<sup>[7]</sup> S50<sup>[7]</sup> and AT11,<sup>[8a]</sup> have been reported to interact with cellular targets, resulting in therapeutic effects through several mechanisms, one example being the inhibition of the anti-apoptotic protein B-cell lymphoma 2 (Bcl-2).<sup>[4b,8b-d]</sup> These G4 aptamers display desirable characteristics such as easy chemical access and modification, high cellular uptake and serum stability, and low immunogenicity.<sup>[9]</sup> Although G4 aptamers exhibit specific recognition properties and potential therapeutic activity,<sup>[4-9]</sup> their application is limited due to the complex tumor microenvironment, which makes them difficult to deploy in a standardized manner. To address this challenge, we present the design, synthesis and use of a multifunctional nanomaterial as a theranostic agent.

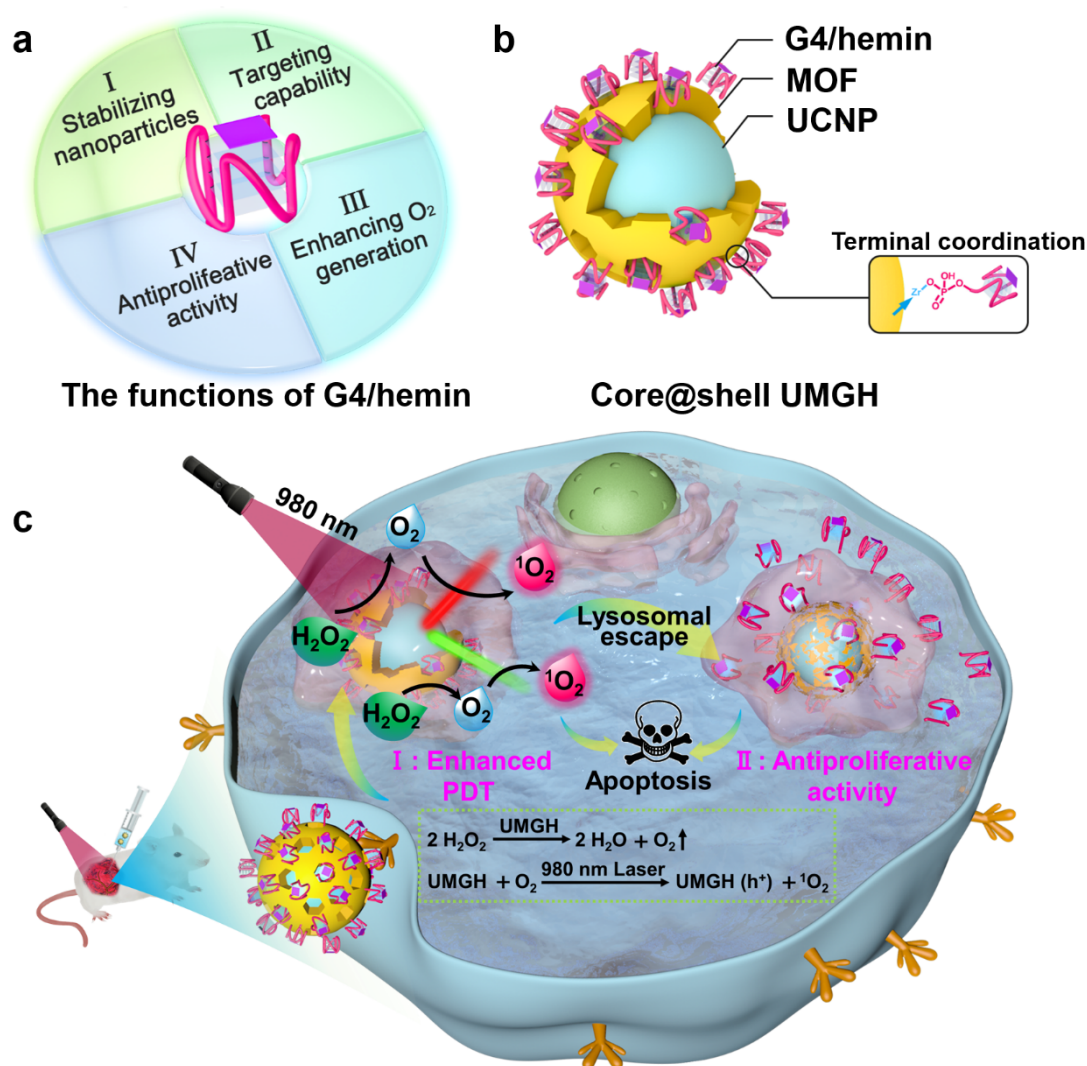
Nanomaterials such as metal-based nanospheres, carbon nanotubes and metal-organic frameworks (MOFs)<sup>[10]</sup> functionalized with DNAs are gaining widespread use in nanobiotechnology. MOFs in particular are highly desirable nanocarriers owing to their easy synthetic access, controllable pore size, large specific surface area, low cytotoxicity and good biocompatibility, making them suitable for drug delivery, catalysis and biosensing applications.<sup>[3b,11]</sup> Moreover, by coating them with G4-forming aptamers such as AS1411, MOFs can be used to specifically target cancer cells through the interaction between aptamers and cell-surface G4-affinity receptors, such as nucleolin.<sup>[12]</sup> Porphyrinic MOFs can even be used in photodynamic therapy (PDT) as they enable increasing loading of photosensitizers (PSs).<sup>[13]</sup> However, a limitation to the broader use of PDT with porphyrin-coated MOFs lies in the necessity of visible

light activation, which restricts tissue penetration. To overcome this problem, near-infrared (NIR) light irradiation would be a preferable option, thanks to its deeper tissue penetration and lower induced tissue damage.<sup>[14]</sup> Consequently, upconversion luminescence nanoparticles (UCNPs) are viewed as the best option for converting NIR light to the visible spectrum, thus enabling NIR-promoted PDT through fluorescence energy resonance transfer (FRET) between UCNP and MOFs.<sup>[15]</sup> However, the efficiency of O<sub>2</sub>-dependent PDT is hindered by the highly hypoxic microenvironment found in solid tumors.<sup>[16]</sup>

To produce O<sub>2</sub> in situ, nanomaterial-based catalysts employing either natural (*e.g.*, catalase) or artificial enzymes (*e.g.*, nanozymes) are commonly used, since they are capable of producing oxygen in areas with higher concentrations of H<sub>2</sub>O<sub>2</sub> such as tumors.<sup>[17a,b]</sup> The use of catalase, in spite of its high efficiency for the conversion of H<sub>2</sub>O<sub>2</sub> into O<sub>2</sub> in tumor tissues, is limited by its physiological instability.<sup>[17c]</sup> Nanozymes, such as ion-doped nanozymes (Fe<sup>III</sup>-C<sub>3</sub>N<sub>4</sub> nanosheets),<sup>[17d]</sup> composite nanozymes (Prussian blue),<sup>[17e]</sup> MOF nanozymes (MIL-100 (Fe))<sup>[17f]</sup> and precious metal nanozymes (Pt, Au@Rh),<sup>[17g,h]</sup> offer higher efficiencies, but their synthesis and colloidal stability are more complex. Recently, the Liu group developed a polymer comprising AS1411, hemin and chlorin e6 (Ce6), that can effectively convert tumor endogenous H<sub>2</sub>O<sub>2</sub> into O<sub>2</sub> mimicking catalase in its action, and proved to be effective for PDT.<sup>[18]</sup>

This system has the potential for further improvement. To capitalize on this, we have taken the best elements from the approaches previously mentioned. As shown in **Scheme 1**, we designed and constructed a G4 DNA termed AS1411-A (d-(G<sub>2</sub>T)<sub>4</sub>TG(TG<sub>2</sub>)<sub>4</sub>A), derived from AS1411, which has already entered clinical trials for cancer therapy.<sup>[4c,4d,9a]</sup> While preserving the attractive properties of AS1411 (*i.e.*, targeting cancer cells, stabilizing nanoparticles, antiproliferative activity), AS1411-A exhibited a substantially increased efficiency (*ca.* 100% increase) of converting H<sub>2</sub>O<sub>2</sub> to O<sub>2</sub> in the presence of hemin when compared to AS1411 (further elaborated on below). Then, we anchored the AS1411-A/hemin complex on the surface and pores of the core-shell UCNP@porphyrinic MOF (referred to as UMGH) with the aim of using this

construct to fight hypoxic tumors via a combined action of enhanced PDT and antiproliferative activity. Upon irradiation at 980 nm (NIR region), a FRET phenomenon enabled the sensitization of the porphyrinic MOF, resulting in the generation of singlet oxygen ( $^1\text{O}_2$ ). This PDT activity, when combined with the anticancer activity of AS1411-A, created a nanoplatform with a high efficiency against hypoxic tumors, as demonstrated here *in vivo*. These findings allow us to broaden the possible use of G4s in resolutely multidisciplinary fields, with the UMGH developed here representing a novel kind of theranostics agent.



**Scheme 1.** Schematic illustration of (a) the roles of G4/hemin complexes in the present work, (b) the core-shell UMGH nanoplatform, and (c) the antitumor mechanism of UMGH nanoplatform. Hemin is represented by a purple square, and G-quadruplex/hemin is expressed as G4/hemin; UCNP stands for upconversion luminescence nanoparticle, MOF for metal-organic framework, and the G4/hemin functionalized core-shell UCNP@MOF is referred to as the UMGH nanoplatform.

## 2. Results and Discussion

### 2.1. Synthesis and Characterization of UMGH NPs

We synthesized the core-shell upconverted metal-organic framework (UMOF) with an individual UCNP as the core and porphyrin MOF as the shell, using a heterogeneous nucleation approach.<sup>[19]</sup> We then functionalized the UMOF with the G4/hemin (GH) complex through a simple coordination approach with the terminal phosphate of G4 and the coordination of unsaturated Zr sites in UMOF (**Figure 1a**). In more detail, the initial core of the uniform UCNP was stabilized by oleic acid (OA-UCNP) with an average size distribution of *ca.* 29 nm, as evaluated by powder X-ray diffraction (PXRD) and transmission electron microscopy (TEM) imaging (**Figure S1**). We removed the oleic acid (OA) with nitrosonium tetrafluoroborate (NOBF<sub>4</sub>),<sup>[20]</sup> then coated the surface of UCNP with 3,4-dihydroxyhydrocinnamic acid to form DHCA-UCNP (**Figure 1b**) and PCN-222 (one Zr MOF) precursors, with tetrakis (4-carboxyphenyl) porphyrin (H<sub>2</sub>TCPP) and metal ions (Zr (IV)).<sup>[19]</sup> As Zr (IV) tended to adsorb on the surface of DHCA-UCNP by virtue of the strong interaction with the carboxylic acid groups of DHCA-UCNP, nucleation and growth of Zr MOF was conducted on the surface of the DHCA-UCNP for the formation of core-shell UCNP@MOF heterostructures (UMOF). As shown in **Figure 1c**, TEM indicated an average diameter of approximately 59 nm with a near 100% encapsulation efficiency for the UMOF. Scanning electron microscopy (SEM) and elemental mapping demonstrated a uniform distribution of elements (Y, Yb and Zr) within the core-shell nanospheres (**Figure S2**).

Next, the core-shell UMOF with coordinatively unsaturated metal sites were functionalized with terminal phosphate-modified GH to form core-shell UMGH.<sup>[21]</sup> An excess of GH was added to the dispersed UMOF and incubated for 24 h at room temperature for the functionalization experiment. The GH loading efficiency was evaluated by UV-Vis absorbance changes in the supernatant before and after functionalization using the corresponding calibration curve of G4 DNA (**Figure S3**). This efficiency was determined to be as high as  $4.01 \pm 0.26$  wt %, indicative of higher

loading capacity than our previous system with MIL-53 (Fe).<sup>[3b]</sup> TEM and SEM analyses confirmed the core-shell geometry of UMGH (**Figures 1d** and **S4**). A PXRD analysis further established that the crystalline structure UMOF was unaffected by GH functionalization (**Figure S5**).<sup>[22]</sup> Both energy dispersive X-ray elemental mapping and EDS line scan of UMGH confirmed that Yb, Zr, P, and Fe elements were homogeneously distributed throughout the core-shell spheres (**Figures 1e** and **S6**) testifying to the presence of two additional elements (P and Fe) belonging to the GH complex (**Scheme 1b**). Further verification of the proper formation of UMGH was provided by Fourier-transform infrared (FT-IR) analyses of GH, UMOF and UMGH. As shown in **Figure S7**, UMOF-containing samples displayed the characteristic peaks of Zr-O bonds ( $655\text{ cm}^{-1}$ ),<sup>[23a,b]</sup> and GH-containing samples showed a peak at  $1056\text{ cm}^{-1}$  corresponding to the C-N group of hemin,<sup>[23c]</sup> thereby confirming the successful formation of UMGH.

Further information about the UMOF/GH interaction was obtained through photoelectron spectroscopy (XPS) measurements: as depicted in **Figure 1f**, XPS analyses demonstrated the presence of C, Zr and O elements within the UMOF, and of two additional elements (P and Fe) in UMGH, confirming that GH complexes were



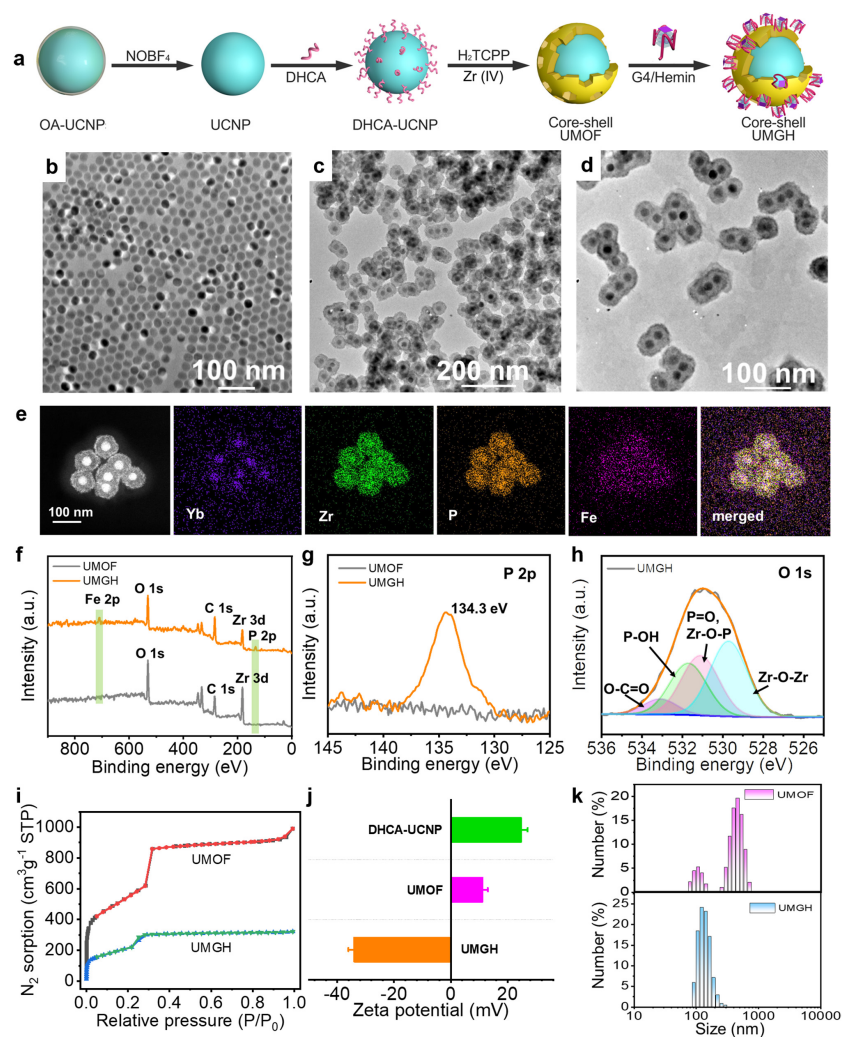


**Figure 1.** Preparation and characterization of UMGH nanostructures. **(a)** Schematic illustration of the synthesis of core-shell UMGH starting from oleic acid-capped UCNP (OA-UCNP). **(b-d)** TEM images of **(b)** DHCA-UCNP, **(c)** core-shell UMOF and **(d)** core-shell UMGH. **(e)** Energy dispersive X-ray elemental mapping of UMGH. **(f)** Photoelectron spectroscopy (XPS) spectra of UMOF before and after modification with GH. **(g-h)** High-resolution XPS spectra of **(g)** P 2p and **(h)** O 1s. **(i)** N<sub>2</sub> adsorption and desorption isotherms for UMOF and UMGH. **(j)** Zeta ( $\zeta$ ) potential of DHCA-UCNP, UMOF and UMGH. **(k)** Dynamic light scattering (DLS) size distribution of UMOF and UMGH in aqueous solution (5-h incubation).

efficiently grafted on the outer surface of the UMOF. In more detail, the typical P peak (2p, 134.3 eV) was absent in UMOF and present in UMGH (**Figure 1g**), indicative of the addition of GH on UMOF. Compared to UMOF, the Zr (3d) peak of UMGH underwent a redshift due to the greater electronegativity of P as compared to Zr and the formation of a Zr-O-P bond between G4 and UMOF that weakens the density of the electron cloud around Zr atoms (**Figure S8a**), leading to a decrease in the shielding

effect on external electrons, thus boosting the binding energy of internal electrons.<sup>[24]</sup> The peak O (1s) in UMGH further proved that GH/UMOF connection through P-O-Zr bond (531.3 eV) (**Figure 1h**).<sup>[24]</sup> In addition, the interactions between UMOF and tripolyphosphate (STPP) were compared and analyzed because Zr MOFs could form Zr-O-P bonds with inorganic phosphates.<sup>[24]</sup> As shown in **Figure S8b**, similar variations of O (1s) XPS spectra indicated that GH bound with UMOF through Zr-O-P bonds. Finally, the Fe (2p) spectrum was analyzed (**Figure S8c**), displaying peaks at 710.6, 716.8, 711.2 and 725.1 eV, which were attributed to Fe<sup>0</sup> 2p<sub>3/2</sub>, Fe<sup>0</sup> 2p<sub>1/2</sub>, Fe-N 2p<sub>3/2</sub> and Fe-N 2p<sub>1/2</sub>, respectively, thus implying the presence of hemin within UMOF.<sup>[22b,25]</sup>

To further characterize the surface area and pore size of both UMOF and UMGH, the nitrogen adsorption-desorption isotherm was measured: as seen in **Figure 1i**, the Brunauer-Emmett-Teller (BET) surface area decreased from unfunctionalized UMOF (1,976 m<sup>2</sup>/g) to UMGH (984 m<sup>2</sup>/g), which was attributed to the GH loading within the pores of UMOF. Additionally, their pore size distributions were around 27 Å while the pore volume of UMGH decreased markedly when compared with that of UMOF, suggesting partial pore filling by GH complexes (**Figure S9a**). These results, together with previous XPS data, indicated that GH complexes are present on the surface as well as within the pores of UMOFs, where their activity is still possible. Additionally, the zeta (ζ) potentials of UCNP, UMOF and UMGH (**Figure 1j**) were +24.7 mV, +11.1 mV and -33.9 mV, respectively, indicating a better dispersion of UMGH in aqueous solution compared to UCNP and UMOF.<sup>[26]</sup> Dynamic light scattering (DLS) measurements showed that UMGH had a larger hydrophilic diameter than UMOF (122 nm vs 105 nm), which again confirmed the GH loading on the surface of UMOF (**Figure 1k**). After a 5-h incubation in an aqueous solution, DLS analyses showed that UMGH exhibited a lower polydispersity (index = 0.281) than UMOF (0.603), proving that GH increased the colloidal stability of UMOF. Moreover, no obvious change in UMGH hydrophilic diameter was found in aqueous solution within one week (**Figure S9b**), indicating the stability of this modification. Collectively, these results demonstrated the successful synthesis of the core-shell UMGH nanoplatfrom, with GH

complexes present both on the surface and inside the pores of the UMOF.

## 2.2. The Functionality of G4/hemin Complex

We then shifted our focus to the catalytic activity of GH complexes. We verified that GH complexes could indeed catalyze the decomposition of H<sub>2</sub>O<sub>2</sub> to produce O<sub>2</sub>, as previously reported.<sup>[18,27]</sup> In an effort to enhance the catalytic performance of the corresponding GH complexes, we optimized the nature of the G4 core (**Figure 2a**). To this end, we studied a series of AS1411 derivatives by optimizing different terminal base compositions (**Table S1**). Circular dichroism (CD) analyses confirmed their G4 structures (**Figure S10**).<sup>[28a]</sup> First, as seen in **Figures 2b** and **S11**, the catalytic

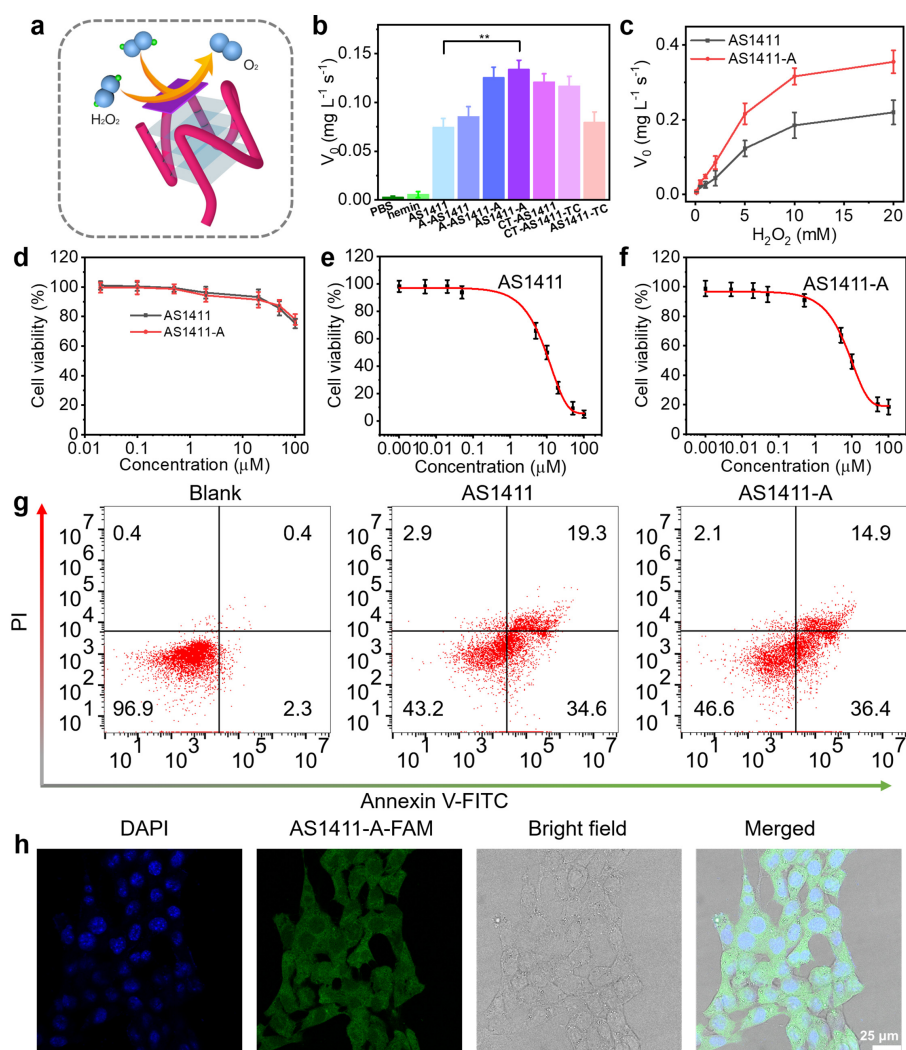


**Figure 2.** Properties of AS1411-A/hemin complexes. (a) Schematic illustration of the conversion of  $\text{H}_2\text{O}_2$  into  $\text{O}_2$  by GH complexes. (b) Initial velocity ( $V_0$ ) of oxygen production in 2.0 mM  $\text{H}_2\text{O}_2$  solutions after adding a series of AS1411 derivatives and hemin. \*\* $p < 0.01$ . (c) Relationship between initial velocity ( $V_0$ ) of oxygen generation and  $\text{H}_2\text{O}_2$  concentration. (d-f) Antiproliferative activity ( $\text{IC}_{50}$ ) of AS1411 derivatives in (d) MCF-10A cells and (e-f) 4T1 cells treated for 96 h. (g) Apoptosis analysis using annexin V-FITC/PI double staining on 4T1 cells either untreated or treated for 96 h with 10  $\mu\text{M}$  AS1411 derivatives, and the proportion of apoptotic cells was the sum of early and late apoptotic cells. (h) Targeting 4T1 breast cancer cells with AS1411-A (from left to right: DAPI and FAM channels, bright field and merged channels).

activities of all AS1411 derivatives (associated with hemin) were found to be significantly enhanced in comparison to the original AS1411. Amongst them, AS1411-A, which had an additional A base at its 3' end, was the most active: its initial velocity ( $V_0$ ) of oxygen production from 2 mM  $\text{H}_2\text{O}_2$  increased to  $0.13 \text{ mg L}^{-1} \text{ s}^{-1}$ , almost double that of AS1411 ( $V_0 = 0.07 \text{ mg L}^{-1} \text{ s}^{-1}$ ). The catalytic activity was further analyzed by

varying the H<sub>2</sub>O<sub>2</sub> concentration: the results seen in **Figure 2c** revealed that the V<sub>0</sub> increased with the increase of H<sub>2</sub>O<sub>2</sub> concentration and that AS1411-A has a superior catalytic activity to AS1411. The catalytic mechanism explaining how H<sub>2</sub>O<sub>2</sub> was converted to O<sub>2</sub> was that hemin bound to G4 was oxidized by H<sub>2</sub>O<sub>2</sub> to form compound I (Fe<sup>IV</sup>=OPor<sup>+</sup>), which further reacted with another molecule of H<sub>2</sub>O<sub>2</sub> to produce O<sub>2</sub>, H<sub>2</sub>O and the regenerated enzyme.<sup>[28b]</sup>

Next, the antiproliferative activities of AS1411 and derivatives on normal cells (MCF-10A) and on a mouse triple-negative breast cancer cell line (4T1) were assessed using the colorimetric methylthiazolyltetrazolium (MTT) assay. The results showed negligible effects on the survival of MCF-10A cells (**Figure 2d**) whereas AS1411 derivatives elicited strong dose-dependent cytotoxic effects on 4T1 cells (**Figures 2e, f** and **S12**). The IC<sub>50</sub> values of AS1411 derivatives were close to that of AS1411 (**Table S2**). To further analyze the ability of AS1411 and AS1411-A to induce cell apoptosis, the apoptotic profile of 4T1 cells with annexin V-FITC/PI double staining was assessed via flow cytometry. The results showed similar properties for AS1411 and AS1411-A, with a proportion of apoptotic cells (the sum of early and late apoptotic cells) of 53.9 and 51.3%, respectively, after incubation with 10 μM AS1411 and AS1411-A for 96 h, respectively (**Figure 2g**).

Finally, we verified the targeting of 4T1 cells by AS1411-A, using optical imaging with a FAM-labeled aptamer and cell adhesion monitored by the confocal laser scanning microscope (CLSM). As seen in **Figure 2h**, the strong green fluorescence within 4T1 cells confirmed the ability of AS1411-A to interact with cancer cells. Collectively, these data demonstrate that the AS1411-A/hemin complex catalyzes the degradation of H<sub>2</sub>O<sub>2</sub> to produce O<sub>2</sub>, stabilizes UMOF in aqueous solution, targets and triggers apoptosis of 4T1 cells.

### 2.3. The Multifunctional UMGH

The functionality of prepared UMGH was thoroughly investigated, predominantly through a cascade catalysis process. This process consisted of two steps, the first being

the production of O<sub>2</sub> from H<sub>2</sub>O<sub>2</sub> and the second being the FRET-mediated production of <sup>1</sup>O<sub>2</sub> (from O<sub>2</sub>). To assess the ability of UMGH to convert H<sub>2</sub>O<sub>2</sub> into O<sub>2</sub>, the amount of O<sub>2</sub> produced by either UMOF or UMGH was measured in solution. **Figure 3a** demonstrates that the dissolved oxygen produced by UMGH increased to 5.88 mg L<sup>-1</sup> in 300 s, which was 8.5 times higher than the amount produced by UMOF. This noteworthy difference confirmed the role of grafted GH in O<sub>2</sub> generation, and was further corroborated by the noticeable O<sub>2</sub> bubbling observed after the addition of UMGH (**Figure S13**).

Next, the energy transfer ability of UMGH was investigated. Under NIR light irradiation (980 nm), the UCNP core harvested low-energy photons and exhibited a relatively broad upconversion luminescence (UCL) emission in the range of 510-565 nm (<sup>2</sup>H<sub>11/2</sub>, <sup>4</sup>S<sub>3/2</sub> → <sup>4</sup>I<sub>15/2</sub>) and 650-675 nm (<sup>4</sup>F<sub>9/2</sub> → <sup>4</sup>I<sub>15/2</sub>).<sup>[29]</sup> This emission aligned with the Q bands (500-700 nm) of the outer porphyrin MOF shells, suggesting a potential energy transfer from the UCNP core to the porphyrin MOF shell (**Figure S14**). Subsequently, the UCL spectra of the UCNP, UMOF and UMGH were measured and analyzed (**Figure 3b**): like UMOF, the emission bands of UMGH suggested an efficient energy transfer from the inner UCNP core to the outer porphyrin MOF shell. To confirm this energy transfer, time-resolved photoluminescence measurements were conducted. As seen in **Figure S15**, the UCL decay curves of UCNP and UMGH showed an obvious reduction from 161 to 94 μs after GH grafting, which can be used to estimate the energy transfer efficiency from UCNP core to the shell within UMGH, which is ca. 42% according to previously described methods.<sup>[22]</sup>

We then determined the effectiveness of UMGH to produce <sup>1</sup>O<sub>2</sub> upon NIR irradiation (980 nm). To this end, we employed the reagent singlet oxygen sensor green (SOSG) to monitor <sup>1</sup>O<sub>2</sub> production in the porphyrin MOF, under both normoxia and hypoxia conditions, with or without laser illumination (0.5 W cm<sup>-2</sup>). As depicted in **Figure 3c**, with UMGH in normoxia conditions, low and high <sup>1</sup>O<sub>2</sub> production was detected before and after 980 nm laser irradiation, respectively, indicating that light is

an active trigger for  $^1\text{O}_2$  production. This generation was much higher than that of MGH (G4/hemin anchored Zr MOF), demonstrating the efficient energy transfer between UCNP core and porphyrinic MOF shell. The  $^1\text{O}_2$  generation of UMGH decreased to 11% under hypoxia conditions (constant  $\text{N}_2$  flush). However, this could be reversed by the addition of  $\text{H}_2\text{O}_2$  (100  $\mu\text{M}$ ), confirming the strong catalytic activity of UMGH to decompose  $\text{H}_2\text{O}_2$  into  $\text{O}_2$ . The  $^1\text{O}_2$  quantum yield ( $\Phi_{\Delta(x)}$ ) of UMGH was determined to be 0.31 using methylene blue (MB) as a standard (**Figure S16**).<sup>[30]</sup> Additionally, electron spin resonance (ESR) experiments were conducted to confirm the production of  $^1\text{O}_2$  and  $\text{O}_2^{\cdot-}$  upon exposure to NIR light. As seen in **Figure 3d**, three characteristic peaks (1:1:1 ratio) were observed in the presence of 2,2,6,6-tetramethyl-4-piperidine (TEMP) to trap  $^1\text{O}_2$  in water under a continuous  $\text{N}_2$  flush and upon irradiation at 980 nm for 30 min in the presence of 100  $\mu\text{M}$   $\text{H}_2\text{O}_2$ . This result was close to these signals detected in normoxia conditions with either UMOF or UMGH, in accordance with the results of **Figure 3c**. As shown in **Figure 3e**, four distinctive peaks (1:1:1:1 ratio) were evident on the spectrum of UMGH in the presence of 5,5-dimethyl-1-pyrroline N-oxide (DMPO) in MeOH solution containing 100  $\mu\text{M}$   $\text{H}_2\text{O}_2$  upon irradiation of 980 nm laser for 30 min, confirming the generation of  $\text{O}_2^{\cdot-}$  radicals. In contrast, a very faint signal was noticed in DMPO in an aqueous solution containing 100  $\mu\text{M}$   $\text{H}_2\text{O}_2$ , suggesting that the production of  $\cdot\text{OH}$  radicals was minimal under these conditions (**Figure 3f**).

MOFs have emerged as promising photocatalysts activated by visible light. This is due to the metallic nodes of MOFs acting as inorganic semiconductors and the bridging organic linkers serving as antennae to harvest light energy and transfer it to the metal clusters.<sup>[31]</sup> Given the semiconductor-like behavior of outer PCN-222 MOF shell in UMGH,<sup>[23a,31a,32]</sup> it is reasonable to assume that upon exposure to NIR light, photo-induced holes ( $\text{h}^+$ ) and electron ( $\text{e}^-$ ) may be generated. The light absorption measurement of UMGH was conducted using UV-Vis diffuse reflectance spectroscopy (DRS) (**Figure S17a**), which revealed the presence of Soret and Q bands belonging to the porphyrins. Since the UCNP core emitted green and red light, the band gaps energy ( $E_g$ ) was determined to be ca. 1.80 eV from DRS spectrum using the Tauc plot method

(Figure S17b). Additionally, Figure S18 demonstrated that the valence band (VB) of UMOF was located at 0.87 eV in the XPS spectrum, and their conduction band (CB) was calculated to be -0.93 eV according to the empirical formula  $E_{CB} = E_{VB} - E_g$ , in agreement with previous findings.<sup>[23a]</sup> On this basis, we can postulate a mechanism (illustrated in Figure 3g) for the catalytic production of  $^1O_2$  by UMGH. We believe that the anchored GH complexes convert  $H_2O_2$  to  $O_2$  with high efficiency; this  $O_2$  is then converted into  $^1O_2$  according to the following cascade: upon irradiation at 980 nm, the UCNP cores emitted green and red light, which is rapidly absorbed by the outer PCN-222 MOF shell, thus creating  $e^-$  and  $h^+$  photogenerated species. These species migrate to the particle surface and collide with  $O_2^{\cdot-}$  radicals (produced concomitantly with  $O_2$ ) to produce  $^1O_2$ . The attractive core-shell UMGH nanoplatform is anticipated to enhance PDT via the *in situ* generation of oxygen.

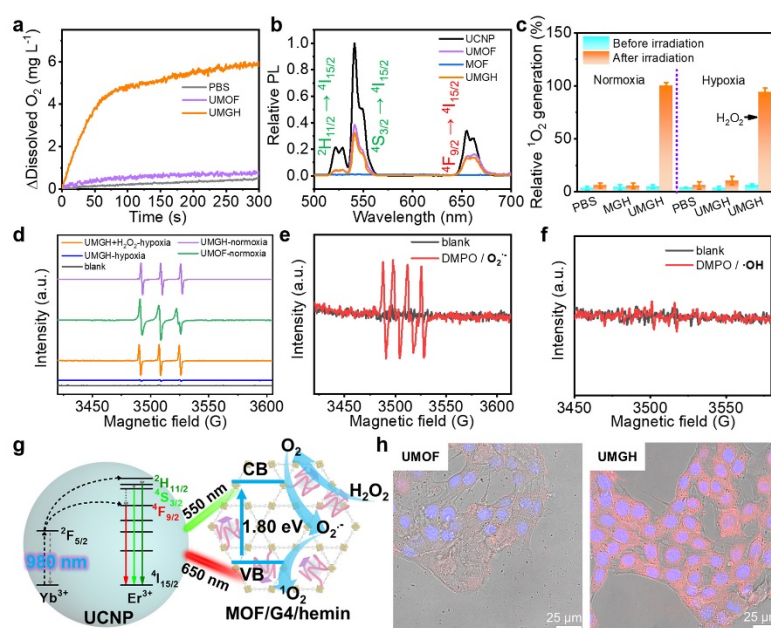


**Figure 3.** Characterizations of UMGH properties: (a)  $O_2$  generation in PBS solution without or with UMOF and UMGH in the presence of  $H_2O_2$ . (b) Luminescence (UCL) emission of UCNP, MOF, UMOF and UMGH. (c) Singlet oxygen ( $^1O_2$ ) production was detected by SOSG indicator under normoxia and hypoxia conditions before and after irradiation. (d-f) Electron spin resonance (ESR) spectra of (d) TEMP-UMGH in aqueous suspension with or without  $H_2O_2$  and (e-f) DMPO- $H_2O_2$ -UMGH in (e) methanol solution and (f) aqueous solution, obtained after irradiation (980 nm) under  $N_2$ . (g) Schematic illustration of the possible mechanism by which UMGH converted  $H_2O_2$  to  $O_2$  and then  $O_2$  is converted to  $^1O_2$  under NIR irradiation. (h) Merged images showing the accumulation of UMOF and UMGH in 4T1 cells after incubation for 8 h at 37 °C. The corresponding images with Hoechst, UMGH and bright field are shown in Figure S19 (supporting information).



The ability of UMGH to target cancer cells was then investigated using optical imaging, which detected the red fluorescence of the UMGH originating from the porphyrin MOF. As illustrated in **Figures 3h** and **S19**, UMGH strongly accumulated in 4T1 cells compared to UMOF, indicating that G4/hemin complexes endowed UMGH with good targeting ability toward cells. It is noteworthy that more black dots are visible in the UMOF image, which may be ascribed to its aggregation outside the cells, further indicating that the presence of GH complexes onto the surface of UMOF improved the stability of the resulting UMGH in DMEM medium. Altogether, these results showed that the simple UMGH nanoplatform can concomitantly trigger the catalytic degradation of H<sub>2</sub>O<sub>2</sub> to produce O<sub>2</sub> and the conversion of O<sub>2</sub> in <sup>1</sup>O<sub>2</sub> under 980 nm irradiation, while also possessing a good targeting ability to cancer cells. This makes the UMGH nanoplatform a good candidate for further biological investigations.

#### **2.4. Therapeutic Activation of UMGH by High Phosphate Concentration**

From a strategic viewpoint, it could be advantageous for the UMGH to gradually degrade in order to liberate GH after it has been internalized. As illustrated in **Figure 4a**, UMGH is degraded in the presence of 10 mM PBS due to the high affinity of Zr (IV) for phosphate ions, which associate to form a low solubility adduct ( $K_{sp} = 10^{-134}$ ).<sup>[33]</sup> TEM images (**Figures 4b, c**) demonstrated that UMGH degraded over 24 h in 10 mM PBS, while it remained stable in the absence of PBS. This degradation was found to be faster in PBS solution than in DMEM (**Figure 4d**). This was confirmed by DLS results, which showed that the hydrodynamic size of UMGH markedly decreased from 122 to 58 nm after being incubated in PBS for 24 h (**Figure 4e**).

We can speculate that in cells, UMGH is degraded during endosome trafficking, where the phosphate concentration is high. This is supported by CLSM images and an endosome/UMGH colocalization experiment (**Figures 4f** and **S20**). After a 3-h incubation of UMGH in 4T1 cells, partial overlap of green (lysotracker, lysosome) and red (UMGH) signals indicated partial colocalization (**Figure S20**). As seen in **Figure**

4f, the UMGH nanopatform is stable in endosomes for 4 h; this is why we decided to expose cells to NIR light (980 nm) for 4 h after the start of the UMGH incubation for subsequent experiments.

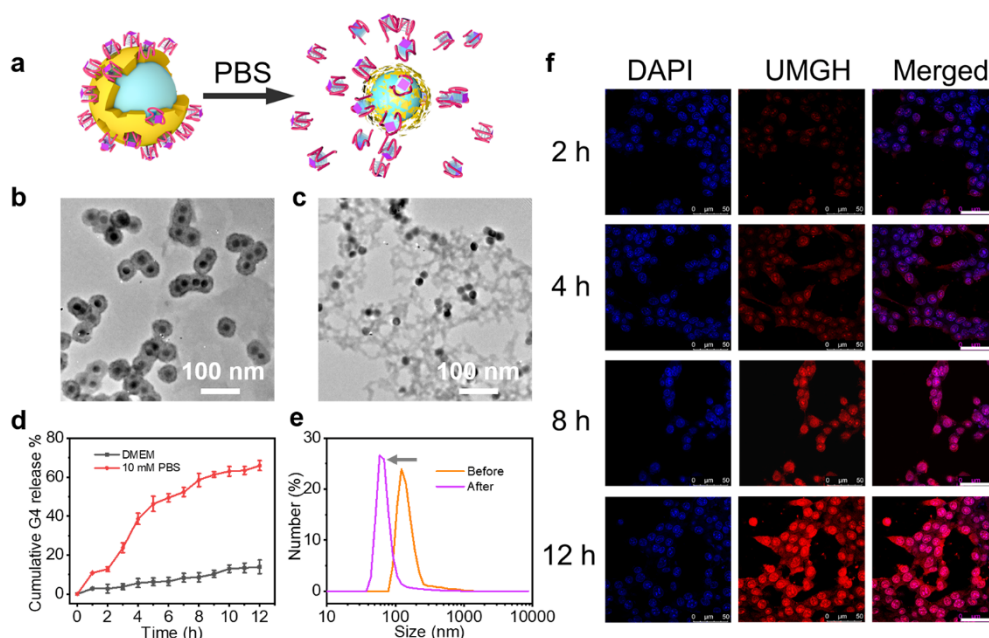


**Figure 4.** (a) Schematic illustration of degradation of UMGH in PBS and release of G4/hemin, which originates in the high affinity of Zr (IV) to phosphate ions. (b and c) TEM images of UMGH before (b) and after (c) incubation with 10 mM PBS solution over 24 h. (d) Degradation profiles of UMGH incubated in either DMEM or 10 mM PBS. (e) Change in size UMGH before (orange) and after (purple) a 24-h incubation in PBS. (f) CLSM images showing the decomposition of UMGH after internalization in 4T1 cells (nuclei stained with DAPI; scale bars: 50  $\mu$ m).

## 2.5. In Vitro Therapy of UMGH

To go a step further, the concentration of  $O_2$  in 4T1 cells incubated with UMGH under hypoxic conditions was assessed through image-iT<sup>TM</sup> green hypoxia reagent. As depicted in **Figure 5a**, both PBS- and UMOF-treated cells exhibited strong green fluorescence; in contrast, after incubation with either GH or UMGH, the fluorescence intensity was strongly decreased, indicating that G4/hemin and UMGH were indeed capable of diminishing hypoxia in cells. The generation of intracellular  $^1O_2$  was also estimated via CLSM imaging (**Figure 5b**): a bright green fluorescence was observed with UMGH- and UMOF-treated cells upon 980-nm irradiation only, the former being

far higher than the latter, indicating the involvement of GH in the conversion of H<sub>2</sub>O<sub>2</sub> into O<sub>2</sub>.

As discussed above, part of AS1411 anticancer activity results from a lowered expression of the Bcl-2 protein.<sup>[9,18]</sup> To verify whether AS1411-A acts in a similar manner, we performed immunoblotting experiments (with GAPDH as internal reference) to measure the expression of Bcl-2 within 4T1 cells upon several treatments. **Figures 5c-d** demonstrated that 4T1 cells incubated with UMOF under NIR irradiation (980 nm) exhibited a slight decrease in Bcl-2 expression, while cells incubated with AS1411-A showed a more significant decrease (*ca.* 58% of the untreated group); similarly, cells incubated with UMGH also experienced a pronounced reduction of Bcl-2 expression following 980 nm light exposure. Additionally, MTT assays were performed to confirm the lack of toxicity of UMOF (cell viability > 93%, **Figure S21a**) and the antiproliferative activity of GH (100 µg mL<sup>-1</sup> UMGH triggered a decrease to 69% of cell viability) for 4T1 cells. In contrast, UMGH had no significant toxicity to MCF-10A cells (**Figure S21b**) owing to the lack of targeting effect. Further, we also observed that NIR irradiation enhanced UMGH toxicity (**Figure 5e**): while the 980-nm irradiation and the incubation of UMOF did not display any toxicity, a 30-min irradiation of cells incubated with UMGH triggered *ca.* 77% of cell death (versus 51% for cells incubated with UMOF). Collectively, these results showed that UMGH could exert its anticancer properties through a combination of ROS production, hypoxia attenuation and GH antiproliferative activity.

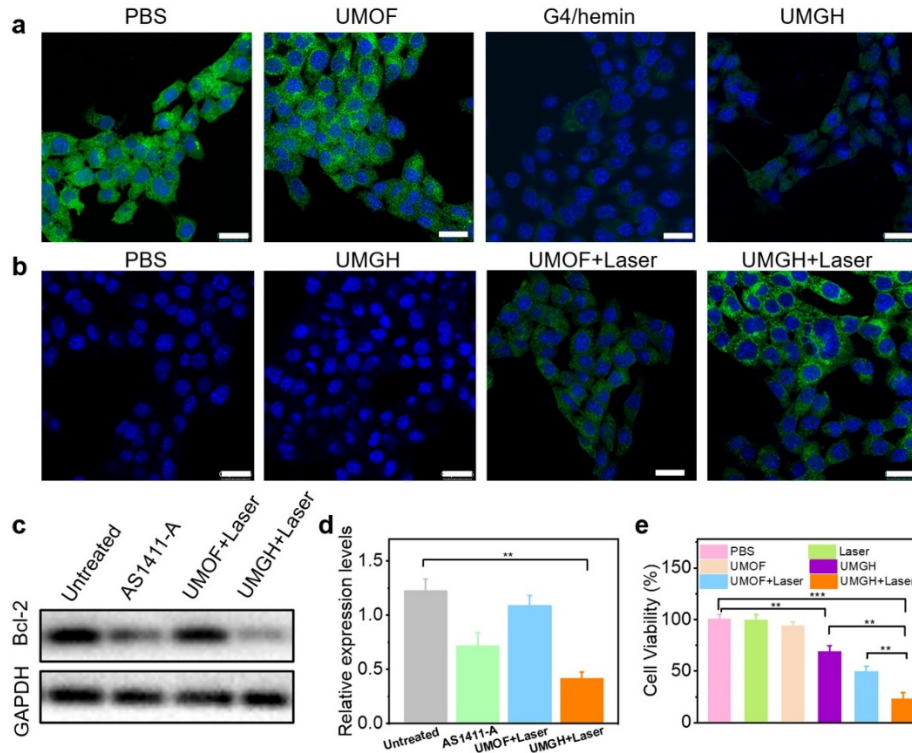


**Figure 5.** In vitro studies of UMGH nanoplateform. (a, b) Intracellular O<sub>2</sub> (a) and <sup>1</sup>O<sub>2</sub> (b) generation by UMOF, GH and UMGH with or without 980-nm irradiation: green signals provided by image-iT<sup>TM</sup> hypoxia reagent (a) and SOSG singlet oxygen indicator (b) (nuclei stained with DAPI; scale bars: 25 μm). (c, d) Western blot (c) and quantified Bcl-2 expression levels (d) from 4T1 cells under different treatments (GAPDH used as internal reference). (e) *In vitro* evaluation of PDT and antiproliferative activity of UMOF and UMGH in 4T1 cells (MTT assay), with and without 980-nm irradiation (0.5 W/cm<sup>2</sup> for 30 min). \*\* p < 0.01, \*\*\* p < 0.001.

## 2.6. In Vivo Therapy of UMGH

Taking into account the promising *in vitro* results of UMGH against 4T1 cell proliferation, its anticancer effects were evaluated on tumor-bearing mice through intratumoral injection. After collecting and measuring the feces and urine within 6 days after injection of UMGH, approximately 72.6% of Y and 75.9% of Zr were excreted through feces and urine analyzed by ICP-MS, respectively, confirming the degradation of UMGH (Figure S22a, b). In comparison to UMOF, Y and Zr accumulation in tumor one day post-injection of UMGH were much higher, demonstrating the tumor targeting ability of UMGH (Figure S22c). We then monitored the tumor volume over a period of 14 days after different treatments. As seen in Figure 6a, the relative tumor volume in the mice treated with either UMGH without laser irradiation or UMOF after laser

illumination was 48% and 29% of that of the control (PBS), confirming the antiproliferative effect of GH within UMGH and of the PDT mediated by UMOF itself. Notably, the tumors in mice treated with UMGH and irradiated were nearly eliminated (decreasing to 5% after 14 days), confirming that UMGH displayed enhanced, multifactorial antiproliferative activity. The survival rate of mice treated with UMGH and laser irradiation was higher than for other groups (**Figure S22d**). No noticeable change in body weight was observed during the treatment, indicating its safety (**Figure 6b**). This remarkable antitumor effect was corroborated by the size of the tumors that were surgically removed from the mice in every group (**Figure 6c**).

Next, the reduction of expression of Bcl-2 was evaluated in tumor slices by a Bcl-2 staining assay (**Figure S23a**): the PBS-treated mice and those treated with UMOF with irradiation exhibited strong and bright Bcl-2 foci whereas those treated with UMGH without irradiation and UMGH with irradiation displayed weak green immunofluorescence only, indicating reduced Bcl-2 levels. We also assessed the changes in hypoxia tracking HIF-1 $\alpha$  (**Figure S23b**): strong immunofluorescence was seen within the PBS-treated and UMOF-treated cells with irradiation, while a low green immunofluorescence was observed within those treated with UMGH without irradiation and UMGH upon irradiation, demonstrating that higher O<sub>2</sub> concentration relieved tumor hypoxia.

Afterwards, hematoxylin and eosin (H&E) staining experiments were performed with tumor slices. This staining (**Figure 6d**) illustrated the serious structure damage triggered by incubation with UMGH, UMOF and UMGH upon laser irradiation, especially in the group of UMGH. Terminal deoxynucleotidyl transferase mediated dUTP-biotin nick end labeling (TUNEL) staining experiments (**Figure 6e**) confirmed these results, showing that the UMGH-treated group with irradiation had the highest apoptosis level.<sup>[18,22b]</sup> Both H&E and TUNEL experiments explained the drastic decrease of the tumor size after intratumoral injection of UMGH, which mediated its activity through strengthened PDT and antiproliferative activity of released AS1411-A, which translated into the tumor growth curves seen in **Figure 6a**. Furthermore, the lack

of apparent pathological abnormalities within other major organs (**Figure S24**) reaffirmed the potential of UMGH as a PDT agent.

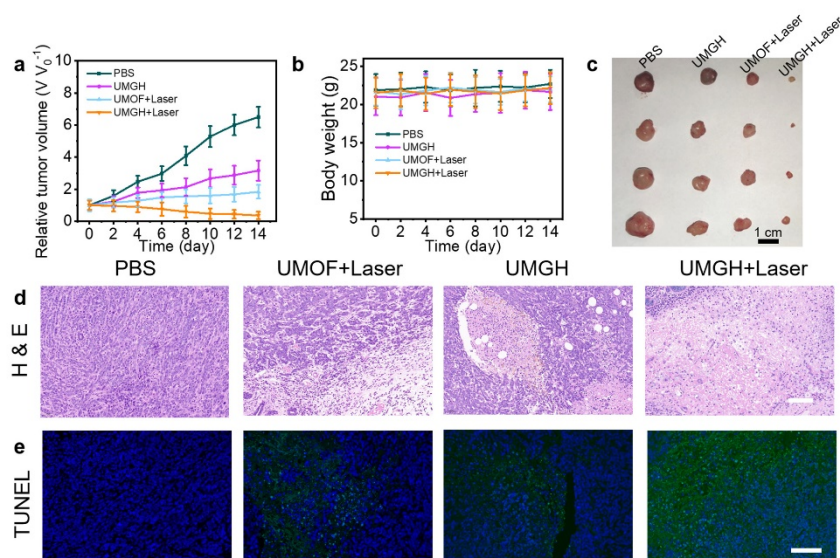


**Figure 6.** Therapeutic effect of UMGH by intratumoral injection in mice. (**a-c**) Tumor growth curves (**a**) and body weight changes (**b**) of 4T1 tumor-bearing BALB/c mice under different treatments over 14 days. (**c**) Images of tumors were collected from 4 groups of mice after different treatments for 14 days. (**d, e**) H&E stained images (**f**) and (**g**) TUNEL assays of tumor slices collected from 4T1 tumor-bearing mice treated with PBS, UMOF + laser, UMGH, UMGH and irradiation (scale bars: 100  $\mu$ m).

### 3. Conclusion

In this study, we designed, synthesized and studied a novel G4/hemin (GH) complex that displayed enhanced capacity for catalytically converting  $H_2O_2$  into  $O_2$ , stabilizing nanoparticles, targeting cancer cells, and killing them via an apoptotic pathway. Then, the upconverted MOF (UMOF) was decorated with GH complexes and the resulting core-shell UMGH nanoplatfrom was used to catalyze  $O_2$  formation from  $H_2O_2$  and further catalyze the generation of  $^1O_2$  upon 980 nm NIR irradiation, which was responsible for the enhanced photodynamic therapeutic activity of UMGH. Further, the grafted GH within UMGH endowed it with improved chemical stability, chemotherapeutic activity, enhanced  $O_2$  generation and targeting tumor ability. Compared to most reported platforms, the UMGH system developed here has the advantages of relatively low cost and simple synthesis. Additionally, the chemotherapeutic activity and enhanced PDT of UMGH were validated both *in vitro*

and *in vivo*, and these studies clearly showed that UMGH mediated remarkable antitumor properties. This work thus provides a new landmark in the development of G4-based nanomedicine.

#### 4. Experimental Section

The main experimental procedures are introduced here, while other protocols are shown in supporting information.

*UMGH Synthesis:* The synthesis method of UMGH was based on the reported method of our group with several modifications.<sup>[3b]</sup> Specifically, 2 mL of 1 mg mL<sup>-1</sup> prepared UMOF was dispersed into 2 mL 10 μM G4/hemin solution, with vigorous stirring at room temperature for 24 h. Subsequently, the products were gathered, centrifugated and washed three times with water. Ultimately, the obtained products were redispersed in water with 100 mM KCl for the following use.

*Catalyzing the Decomposition of H<sub>2</sub>O<sub>2</sub> to Generate O<sub>2</sub>:* The oxygen concentration in PBS buffer solution was recorded in real time in the presence of different bio-composites including AS1411/hemin with different sequences, UMOF and UMGH. Briefly, these composites were added in 2.0 mM H<sub>2</sub>O<sub>2</sub> respectively, followed by N<sub>2</sub> blowing for 30 min. The generated O<sub>2</sub> concentration was immediately monitored by a dissolved oxygen analyzer. The PBS with H<sub>2</sub>O<sub>2</sub> was selected as the control group.

*Intracellular Oxygen Generation by UMGH:* Image-iT green hypoxia reagent, whose fluorescence was quenched by O<sub>2</sub> in live cells and tissues, was used as oxygen indicator to monitor the oxygen production with UMGH. In brief, 4T1 cells were pretreated with fresh culture containing UMOF and UMGH for 24 h in hypoxia environment and then the medium was replaced with 5 μM image-iT green hypoxia reagent for another 0.5 h. Then, their confocal fluorescence images were gathered with the emission between 510 and 540 nm under excitation at 488 nm.

*Antiproliferative Activity Test of AS1411 Derivatives:* The antiproliferative effect of AS1411 derivatives was evaluated using typical MTT assays. For the analysis, 4T1

cells were planted in 96-well plates with  $5.0 \times 10^4$  cells in each well and incubated for 24 h at 37 °C. The 4T1 cells were then incubated fresh DMEM medium containing 10  $\mu$ M AS1411 derivatives for another 96 h. Then, 50  $\mu$ L of MTT stock solution (2 mg mL<sup>-1</sup>) was added to each well and incubated for another 4 h. Next, 150  $\mu$ L DMSO was added to dissolve the precipitated formazan after removing the former culture medium. The absorbance at 490 nm was detected on a microplate reader. All samples were prepared in triplicate.

*In Vivo Anticancer Effect in a Subcutaneous Model:* All animal assays were conducted in agreement with the NIH guidelines for the care and use of laboratory animals (NIH Publication no. 85-23 Rev. 1985) and approved by the experimental animal center of Nanjing University of Chinese Medicine (Approval Number: 202208A041). To establish a 4T1 tumor xenograft mouse model, female BALB/c mice (6-8 weeks-old) were inoculated with 4T1 cells ( $1.0 \times 10^6$ ) subcutaneously into the right flank position. After the tumor size reached 70-90 mm<sup>3</sup>, 4T1 tumor bearing mice were randomly divided into four groups and treated as follows: (i) PBS, (ii) UMGH, (iii) UMOF with laser irradiation, (iv) UMGH with laser irradiation. UMOF and UMGH were injected intratumorally at a concentration of 2 mg mL<sup>-1</sup>. In the experiments, tumors at 4 h post-injection were irradiated by the 980 nm laser (0.6 W/cm<sup>2</sup>) for 30 min with 5 min breaks after every 5 min irradiation. The injection and treatment were repeated with the same procedure on days 2, 4, 8 and 12. Tumor size was measured with a vernier caliper every two days and calculated by the formula (length  $\times$  width  $\times$  width)/2. The body weight of each mouse was recorded every two days. Tumors and major organs (heart, liver, spleen, lung, and kidney) were sectioned for hematoxylin-eosin staining (H&E), TUNEL analysis and immunofluorescence analyses at the end of the experiment.

### **Supporting Information**

Supporting Information is available from the Wiley Online Library or from the authors.



## **Acknowledgements**

The authors acknowledge the financial support of the National Natural Science Foundation of China (21977045, 22177047, 22004062, and 22104063), the Fundamental Research Funds for the Central Universities (020514380299, 202200324 and 202200325), State Key Laboratory of Analytical Chemistry for Life Science (5431ZZXM2202 and SKLACLS2109, SKLACLS2307), China Postdoctoral Science Foundation (2021M702106), Agence Nationale de la Recherche (ANR G4Access [ANR-20-CE12-0023]) and INCa PL-Bio (G4Access).

## **Conflict of Interest**

The authors declare no conflict of interest.

## **ORCID identification numbers**

Xiaobo Zhang: [orcid.org/0000-0003-0222-2515](https://orcid.org/0000-0003-0222-2515)

Dehui Qiu: [orcid.org/0000-0002-0085-6832](https://orcid.org/0000-0002-0085-6832)

David Monchaud: [orcid.org/0000-0002-3056-9295](https://orcid.org/0000-0002-3056-9295)

Huangxian Ju: [orcid.org/0000-0002-6741-5302](https://orcid.org/0000-0002-6741-5302)

Jean-Louis Mergny: [orcid.org/0000-0003-3043-8401](https://orcid.org/0000-0003-3043-8401)

Jianping Lei: [orcid.org/0000-0002-3594-180X](https://orcid.org/0000-0002-3594-180X)

Jun Zhou: [orcid.org/0000-0002-6793-3169](https://orcid.org/0000-0002-6793-3169)

## References

- [1] J. L. Mergny, D. Sen, *Chem. Rev.* **2019**, *119*, 6290-6325. DOI:10.1021/acs.chemrev.8b00629
- [2] a) E. Y. N. Lam, D. Beraldi, D. Tannahill, S. Balasubramanian, *Nat. Commun.* **2013**, *4*, 1796; DOI:10.1038/ncomms2792 b) H. Y. Liu, Q. Zhao, T. P. Zhang, Y. Wu, Y. X. Xiong, S. K. Wang, Y. L. Ge, J. H. He, P. Lv, T. M. Ou, J. H. Tan, D. Li, L. Q. Gu, J. Ren, Y. Zhao, Z. S. Huang, *Chem. Biol.* **2016**, *23*, 1261-1270; DOI:10.1016/j.chembiol.2016.08.013 c) G. Biffi, D. Tannahill, J. Miller, W. J. Howat, S. Balasubramanian, *PLoS One* **2014**, *9*, e102711; DOI:10.1371/journal.pone.0102711 d) R. Hansel-Hertsch, D. Beraldi, S. V. Lensing, G. Marsico, K. Zyner, A. Parry, M. D. Antonio, J. Pike, H. Kimura, M. Narita, D. Tannahill, S. Balasubramanian, *Nat. Genet.* **2016**, *48*, 1267-1272; DOI:10.1038/ng.3662 e) J. Spiegel, S. Adhikari, S. Balasubramanian, *Trends Chem.* **2020**, *2*, 123-136. DOI:10.1016/j.trechm.2019.07.002
- [3] a) A. Abiri, M. Lavigne, M. Rezaei, S. Nikzad, P. Zare, J. L. Mergny, H. R. Rahimi, *Pharmacol. Rev.* **2021**, *73*, 897-923; DOI:10.1124/pharmrev.120.000230 b) X. X. Mao, F. N. He, D. H. Qiu, S. J. Wei, R. G. Luo, Y. Chen, X. B. Zhang, J. P. Lei, D. Monchaud, J. L. Mergny, H. X. Ju, J. Zhou, *Anal. Chem.* **2022**, *94*, 7295-7302. DOI: 10.1021/acs.analchem.2c00600
- [4] a) C. R. Ireson, L. R. Kelland, *Mol. Cancer Ther.* **2006**, *5*, 2957-2962; DOI:10.1158/1535-7163.MCT-06-0172 b) P. J. Bates, D. A. Laber, D. M. Miller, S. D. Thomas, J. O. Trent, *Exp. Mol. Pathol.* **2009**, *86*, 151-164. DOI:10.1016/j.yexmp.2009.01.004 c) P. J. Bates, E. M. Reyes-Reyes, M. T. Malik, E. M. Murphy, M. G. O. Toole, J. O. Trent, *BBA Gen. Subj.* **2017**, *1861*, 1414-1428. DOI: 10.1016/j.bbagen.2016.12.015 d) R. Yazdian-Robati, P. Bayat, F. Oroojalian, M. Zargari, M. Ramezani, S. M. Taghdisi, K. Abnous, *Int. J. Biol. Macromol.* **2020**, *155*, 1420-1431. DOI: 10.1016/j.ijbiomac.2019.11.118
- [5] C. Riccardi, E. Napolitano, C. Platella, D. Musumeci, D. Montesarchio, *Pharmacol. Ther.* **2021**, *217*, 107649. DOI: 10.1016/j.pharmthera.2020.107649
- [6] E. M. Garcia-Recio, C. Pinto-Diez, M. I. Perez-Morgado, M. Garcia-Hernandez, G. Fernandez, M. E. Martin, V. M. Gonzalez, *Mol. Ther. Nucleic Acids* **2016**, *5*, e275. DOI:10.1038/mtna.2015.50
- [7] J. Hu, Z. L. Zhao, Q. L. Liu, M. Ye, B. Q. Hu, J. Wang, W. H. Tan, *Chem. Asian J.* **2015**, *10*, 1519-1525. DOI:10.1002/asia.201500187
- [8] a) N. Q. Do, W. J. Chung, T. H. A. Truong, B. Heddi, A. T. Phan, *Nucleic Acids Res.* **2017**, *45*, 7487-7493; DOI:10.1093/nar/gkx274 b) T. K. Sengupta, S. Bandyopadhyay, D. J. Fernandes, E. K. Spicer, *J. Biol. Chem.* **2004**, *279*, 10855-10863; DOI: 10.1074/jbc.M309111200 c) Y. Otake, T. K. Sengupta, S. Bandyopadhyay, E. K. Spicer, D. J. Fernandes, *Mol. Pharmacol.* **2005**, *67*, 319-326; DOI: 10.1124/mol.104.006080 d) S. Soundararajan, W. W. Chen, E. K. Spicer, N. Courtenay-Luck, D. J. Fernandes, *Cancer Res.* **2008**, *68*, 2358-2365. DOI:10.1158/0008-5472.CAN-07-5723
- [9] a) J. Carvalho, J. L. Mergny, G. F. Salgado, J. A. Queiroz, C. Cruz, *Trends Mol.*

- Med.* **2020**, *26*, 848-861; DOI:10.1016/j.molmed.2020.05.002 b) C. Roxo, W. Kotkowiak, A. Pasternak, *Molecules* **2019**, *24*, 3781. DOI: 10.3390/molecules24203781.
- [10] a) D. Q. Fan, J. Wang, E. K. Wang, S. J. Dong, *Adv. Sci.* **2020**, *7*, 2001766; DOI:10.1002/advs.202001766 b) H. X. Zhao, L. H. Li, F. Li, C. X. Liu, M. X. Huang, J. Li, F. Gao, X. H. Ruan, D. Y. Yang, *Adv. Mater.* **2022**, *34*, 2109920; DOI:10.1002/adma.202109920 c) J. J. Shi, W. M. Nie, X. Zhao, X. Y. Yang, H. Cheng, T. H. Zhou, Y. Zhang, K. X. Zhang, J. J. Liu, *Adv. Mater.* **2022**, *34*, 2201049. DOI:10.1002/adma.202201049
- [11] a) P. H. Tong, L. Zhu, Y. Zhang, J. Li, X. P. He, T. D. James, *Chem. Commun.* **2021**, *57*, 12098-12110; DOI: 10.1039/D1CC05157A. b) S. Q. Dong, Q. X. Chen, W. Li, Z. Jiang, J. B. Maa, H. Gao, *J. Mater. Chem. B* **2017**, *5*, 8322-8329; DOI: 10.1039/C7TB01966A c) S. Mallakpour, E. Nikkhoo, C. M. Hussain, *Coord. Chem. Rev.* **2022**, *451*, 214262. DOI: 10.1016/j.ccr.2021.214262. d) B. Liu, M. Jiang, D. Z. Zhu, J. M. Zhang, G. Wei, *Chem. Eng. J.* **2022**, *428*, 131118. DOI: 10.1016/j.ccej.2021.131118
- [12] a) J. C. Yan, T. Gao, Z. Z. Lu, J. B. Yin, Y. Zhang, R. J. Pei, *ACS Appl. Mater. Interfaces* **2021**, *13*, 27749-27773; DOI:10.1021/acsami.1c06818 b) X. Zhao, K. X. Zhang, Y. Y. Wang, W. X. Jiang, H. Cheng, Q. W. Wang, T. T. Xiang, Z. Z. Zhang, J. J. Liu, J. J. Shi, *Adv. Funct. Mater.* **2022**, *32*, 2108883. DOI:10.1002/adfm.202108883 c) W. Morris, W. Briley, E. Auyeung, M. Cabezas and C. A. Mirkin, *J. Am. Chem. Soc.* **2014**, *136*, 7261-7264; DOI:10.1021/ja503215w
- [13] a) W. Zhang, J. Lu, X. Gao, P. Li, W. Zhang, Y. Ma, H. Wang, B. Tang, *Angew. Chem. Int. Ed.* **2018**, *57*, 4891-4896; DOI:10.1002/anie.201710800 b) Y. Ma, X. Y. Li, A. J. Li, P. Yang, C. Y. Zhang, B. Tang, *Angew. Chem. Int. Ed.* **2017**, *56*, 13752-13756; DOI:10.1002/anie.201708005 c) J. Park, Q. Jiang, D. W. Feng, L. Q. Mao, H. C. Zhou, *J. Am. Chem. Soc.* **2016**, *138*, 3518-3525. DOI:10.1021/jacs.6b00007
- [14] a) K. R. Deng, C. X. Li, S. S. Huang, B. G. Xing, D. Y. Jin, Q. G. Zeng, Z. Y. Hou, J. Lin, *Small* **2017**, *13*, 1702299; DOI:10.1002/smll.201702299 b) Y. Z. Shen, A. J. Shuhendler, D. J. Ye, J. J. Xu, H. Y. Chen, *Chem. Soc. Rev.* **2016**, *45*, 6725-6741. DOI:10.1039/C6CS00442C
- [15] T. X. Gu, L. Cheng, F. Gong, J. Xu, X. Li, G. R. Han, Z. Liu, *ACS Appl. Mater. Interfaces* **2018**, *10*, 15494-15503. DOI:10.1021/acsami.8b03238
- [16] a) X. S. Li, N. Kwon, T. Guo, Z. Liu, J. Yoon, *Angew. Chem. Int. Ed.* **2018**, *57*, 11522-11531; DOI:10.1002/anie.201805138 b) L. Huang, S. Zhao, J. Wu, L. Yu, N. Singh, K. Yang, M. H. Lan, P. F. Wang, J. S. Kim, *Coordin. Chem. Rev.* **2021**, *438*, 213888. DOI:10.1016/j.ccr.2021.213888
- [17] a) Y.L. Wan, L. H. Fu, C. Y. Li, J. Lin, P. Huang, *Adv. Mater.* **2021**, *33*, 2103978. DOI: 10.1002/adma.202103978 b) L. R. Zhao, C. H. Fu, L. F. Tan, T. Li, H. S. Zhong, X. W. Meng, *Nanoscale* **2020**, *12*, 2855-2874. DOI: 10.1039/c9nr09071a c) D. Hu, L. Zhong, M. Wang, H. Li, Y. Qu, Q. Liu, R. Han, L. Yuan, K. Shi, J. Peng, Z. Qian, *Adv. Funct. Mater.* **2019**, *29*, 1806199. DOI:

- 10.1002/adfm.201806199 d) Z. F. Ma, M. C. Zhang, X. D. Jia, J. Bai, Y. D. Ruan, C. Wang, X. P. Sun, X. Jiang, *Small* **2016**, *12*, 5477-5487. DOI: 10.1002/sml.201601681 e) J. Zhou, M. H. Li, Y. H. Hou, Z. Luo, Q. F. Chen, H. X. Cao, R. L. Huo, C. C. Xue, L. Sutrisno, L. Hao, Y. Cao, H. T. Ran, L. Lu, K. Li, K. Y. Cai, *ACS Nano* **2018**, *12*, 2858-2872. DOI: 10.1021/acsnano.8b00309 f) F. Hu, D. Mao, Kenry, Y. X. Wang, W. B. Wu, D. Zhao, D. L. Kong, B. Liu, *Adv. Funct. Mater.* **2018**, *28*, 1707519. DOI: 10.1002/adfm.201707519 g) X. S. Wang, J. Y. Zeng, M. K. Zhang, X. Zeng, X. Z. Zhang, *Adv. Funct. Mater.* **2018**, *28*, 1801783. DOI: 10.1002/adfm.201801783 h) J. P. Wang, J. Y. Sun, W. Hu, Y. H. Wang, T. Chou, B. L. Zhang, Q. Zhang, L. Ren, H. J. Wang, *Adv. Mater.* **2020**, *32*, 200186. DOI: 10.1002/adma.202001862
- [18] Y. Yang, W. J. Zhu, L. Z. Feng, Y. Chao, X. Yi, Z. L. Dong, K. Yang, W. H. Tan, Z. Liu, M. W. Chen, *Nano Lett.* **2018**, *18*, 6867-6875. DOI:10.1021/acs.nanolett.8b02732
- [19] Y. Liu, Y. Yang, Y. J. Sun, J. B. Song, N. G. Rudawski, X. Y. Chen, W. H. Tan, *J. Am. Chem. Soc.* **2019**, *141*, 7407-7413. DOI:10.1021/jacs.9b01563
- [20] A. G. Dong, X. C. Ye, J. Chen, Y. J. Kang, T. Gordon, J. M. Kikkawa, C. B. Murray, *J. Am. Chem. Soc.* **2011**, *133*, 998-1006. DOI:10.1021/ja108948z
- [21] S. Z. Wang, C. M. McGuirk, M. B. Ross, S. Y. Wang, P. C. Chen, H. Xing, Y. Liu, C. A. Mirkin, *J. Am. Chem. Soc.* **2017**, *139*, 9827-9830. DOI:10.1021/jacs.7b05633
- [22] a) D. W. Feng, Z. Y. Gu, J. R. Li, H. L. Jiang, Z. W. Wei, H. C. Zhou, *Angew. Chem.* **2012**, *124*, 10453 -10456. DOI: 10.1002/ange.201204475. b) L. C. He, Q. Q. Ni, J. Mu, W. P. Fan, L. Liu, Z. T. Wang, L. Li, W. Tang, Y. J. Liu, Y. Y. Cheng, L. G. Tang, Z. Yang, Y. Liu, J. H. Zou, W. J. Yang, O. Jacobson, F. Zhang, P. T. Huang, X. Y. Chen, *J. Am. Chem. Soc.* **2020**, *142*, 6822-6832. DOI:10.1021/jacs.0c02497
- [23] a) W. L. Sheng, X. X. Wang, Y. X. Wang, S. L. Chen, X. J. Lang, *ACS Catal.* **2022**, *12*, 11078-11088. DOI:10.1021/acscatal.2c02519 b) J. H. Wang, Y. D. Fan, Y. H. Tan, X. Zhao, Y. Zhang, C. M. Cheng, M. Yang, *ACS Appl. Mater. Interfaces* **2018**, *10*, 36615-36621. DOI:10.1021/acsaami.8b15452 c) L. Gomathi Devi, P. M. Nithya, *Inorg. Chem. Front.* **2018**, *5*, 127-138. DOI: 10.1039/c7qi00590c
- [24] a) K. H. Yu, T. X. Wei, Z. J. Li, J. Y. Li, Z. Y. Wang, Z. H. Dai, *J. Am. Chem. Soc.* **2020**, *142*, 21267-21271. DOI:10.1021/jacs.0c10442 b) A. E. Baumann, X. Han, M. M. Butala, V. S. Thoi, *J. Am. Chem. Soc.* **2019**, *141*, 17891-17899. DOI: 10.1021/jacs.9b09538
- [25] Z. X. Liang, H. Y. Song, S. J. Liao, *J. Phys. Chem. C* **2011**, *115*, 2604-2610; DOI:10.1021/jp1112334
- [26] S. Sen, V. Govindarajan, C. J. Pelliccione, J. Wang, D. J. Miller, E. V. Timofeeva, *ACS Appl. Mater. Interfaces* **2015**, *7*, 20538-20547. DOI: 10.1021/acsaami.5b05864
- [27] a) G. X. Lan, K. Y. Ni, Z. W. Xu, S. S. Veroneau, Y. Song, W. B. Lin, *J. Am.*

- Chem. Soc.* **2018**, *140*, 5670-5673; DOI:10.1021/jacs.8b01072 b) Y. Zang, J. P. Lei, L. Zhang, H. X. Ju, *Anal. Chem.* **2014**, *86*, 12362-12368; DOI:10.1021/ac503741x c) R. Freeman, X. Q. Liu, I. Willner, *J. Am. Chem. Soc.* **2011**, *133*, 11597-11604. DOI:10.1021/ja202639m d) M. M. Dailey, M. C. Miller, P. J. Bates, A. N. Lane, J. O. Trent, *Nucleic Acids Res.* **2010**, *38*, 4877-4888. DOI: 10.1093/nar/gkq166.
- [28] a) C. Riccardi, D. Musumeci, I. R. Krauss, M. Piccolo, C. Irace, L. Paduano, D. Montesarchio, *Int. J. of Biol. Macromol.* **2018**, *118*, 1384-1399. DOI:10.1016/j.ijbiomac.2018.06.137 e) Iwaniuk, E. E.; Adebayo, T.; Coleman, S.; Villaros, C. G.; Nesterova, I. V. *Nucleic Acids Res.* **2023**, *51*, 1600-1607. DOI: 10.1093/nar/gkad031
- [29] F. Wang, X. G. Liu, *J. Am. Chem. Soc.* **2008**, *130*, 5642-5643. DOI: 10.1021/ja800868a
- [30] L. Zhang, J. P. Lei, F. J. Ma, P. H. Ling, J. T. Liu, H. X. Ju, *Chem. Commun.* **2015**, *51*, 10831-10834. DOI:10.1039/C5CC03028E
- [31] a) H. Q. Xu, J. H. Hu, D. K. Wang, Z. H. Li, Q. Zhang, Y. Luo, S. H. Yu, H. L. Jiang, *J. Am. Chem. Soc.* **2015**, *137*, 13440-13443. DOI: 10.1021/jacs.5b08773  
 b) M. Alvaro, E. Carbonell, B. Ferrer, F. X. Llabrés i Xamena, H. Garcia, *Chem. - Eur. J.* **2007**, *13*, 5106-5112. DOI: 10.1002/chem.200601003 c) T. Tachikawa, J. R. Choi, M. Fujitsuka, T. Majima, *J. Phys. Chem. C* **2008**, *112*, 14090-14101. DOI: 10.1021/jp803620v
- [32] a) C. Y. Xu, H. Liu, D. D. Li, J. H. Su, H. L. Jiang, *Chem. Sci.*, **2018**, *9*, 3152-3158. DOI: 10.1039/c7sc05296k b) Y. M. Zhao, Y. Z. Dong, F. T. Lu, C. G. Ju, L. Liu, J. Zhang, B. Zhang, Y. Q. Feng, *J. Mater. Chem. A*, **2017**, *5*, 15380-15389. DOI: 10.1039/c7ta03840b
- [33] C. B. He, K. D. Lu, D. M. Liu, W. B. Lin, *J. Am. Chem. Soc.* **2014**, *136*, 5181-5184. DOI:10.1021/ja4098862

## TOC figure and legend

The G-quadruplex AS1411-A ( $(d-(G_2T)_4TG(TG_2)_4A)$ ) keeps the enticing antiproliferative properties of the parent aptamer AS1411 and produces twice as much  $O_2$  in situ with hemin. This AS1411-A/hemin (GH) is then grafted on upconverted metal-organic framework (UMOF) to construct a UMGH nanoplatform that exhibits efficient anticancer properties combining both antiproliferative and enhanced PDT activities.

Xuanxiang Mao,<sup>1</sup> Xiaobo Zhang,<sup>1</sup> Zhicong Chao,<sup>1</sup> Dehui Qiu,<sup>1</sup> Shijiong Wei,<sup>1</sup> Rengan Luo,<sup>1</sup> Desheng Chen,<sup>1</sup> Yue Zhang,<sup>2</sup> Yun Chen,<sup>1</sup> Yuanjiao Yang,<sup>1</sup> David Monchaud,<sup>3</sup> Huangxian Ju,<sup>1</sup> Jean-Louis Mergny,<sup>1,4,\*</sup> Jianping Lei,<sup>1</sup> Jun Zhou<sup>1,\*</sup>

### A Versatile G-quadruplex (G4)-coated Upconverted Metal-Organic Framework for Hypoxic Tumor Therapy

